

# Dynamics of a Standing Meander of the Subantarctic Front Diagnosed from Satellite Altimetry and Along-Stream Anomalies of Temperature and Salinity

JAN JAAP MEIJER,<sup>a,b</sup> HELEN E. PHILLIPS,<sup>a,c,d</sup> NATHANIEL L. BINDOFF,<sup>a,c,d</sup> STEPHEN R. RINTOUL,<sup>e,f,g,d</sup>  
AND ANNIE FOPPERT<sup>c</sup>

<sup>a</sup> *Institute for Marine and Antarctic Studies, University of Tasmania, Hobart, Tasmania, Australia*

<sup>b</sup> *ARC Centre of Excellence in Climate Extremes, Hobart, Tasmania, Australia*

<sup>c</sup> *Australian Antarctic Program Partnership, Institute for Marine and Antarctic Studies, University of Tasmania, Hobart, Tasmania, Australia*

<sup>d</sup> *Australian Centre for Excellence in Antarctic Science, Hobart, Tasmania, Australia,*

<sup>e</sup> *CSIRO Oceans and Atmosphere, Hobart, Tasmania, Australia,*

<sup>f</sup> *Centre for Southern Hemisphere Ocean Research, Hobart, Tasmania, Australia*

<sup>g</sup> *Australian Antarctic Program Partnership, Hobart, Tasmania, Australia*

(Manuscript received 3 March 2021, in final form 17 January 2022)

**ABSTRACT:** Meanders formed where the Antarctic Circumpolar Current (ACC) interacts with topography have been identified as dynamical hot spots, characterized by enhanced eddy energy, momentum transfer, and cross-front exchange. However, few studies have used observations to diagnose the dynamics of ACC standing meanders. We use a synoptic hydrographic survey and satellite altimetry to explore the momentum and vorticity balance of a Subantarctic Front standing meander, downstream of the Southeast Indian Ridge. Along-stream anomalies of temperature in the upper ocean (150–600 m) show along-stream cooling entering the surface trough and along-stream warming entering the surface crest, while warming is observed from trough to crest in the deeper ocean (600–1500 m). Advection of relative vorticity is balanced by vortex stretching, as found in model studies of meandering currents. Meander curvature is sufficiently large that the flow is in gradient wind balance, resulting in ageostrophic horizontal divergence. This drives downwelling of cooler water along isopycnals entering the surface trough and upwelling of warmer water entering the surface crest, consistent with the observed evolution of temperature anomalies in the upper ocean. Progressive along-stream warming observed between 600 and 1500 m likely reflects cyclogenesis in the deep ocean. Vortex stretching couples the upper and lower water column, producing a low pressure at depth between surface trough and crest and cyclonic flow that carries cold water equatorward in the surface trough and warm water poleward in the surface crest (poleward heat flux). The results highlight gradient–wind balance and cyclogenesis as central to dynamics of standing meanders and their critical role in the ACC momentum and vorticity balance.

**SIGNIFICANCE STATEMENT:** The Antarctic Circumpolar Current (ACC) in the Southern Ocean is a nearly zonal current that encircles Antarctica. It acts as a barrier between warmer water equatorward and colder water poleward. In a few regions where the current encounters strong topographic changes, the current meanders and opens a pathway for heat to travel across the ACC toward Antarctica. We surveyed a meander in the ACC and examined the along-stream change of temperature. In the upper ocean, temperature changes are caused by a vertical circulation, bringing cool water down when entering the surface trough (the part of the meander closest to the equator), and warm water up when exiting the surface trough and entering the surface crest. At depth, cold water is transported equatorward in the surface trough and warm water poleward in the surface crest, leading to a net transport of heat poleward. This study highlights the importance of the secondary circulation within a meander for generating cross-ACC flows and moving heat toward Antarctica.


**KEYWORDS:** Ageostrophic circulations; Baroclinic flows; Convergence/divergence; Cyclogenesis/cyclolysis; Fronts; Mesoscale processes; Ocean dynamics; Rossby waves; Topographic effects; Upwelling/downwelling; In situ oceanic observations; Satellite observations; Ship observations

## 1. Introduction

The Antarctic Circumpolar Current (ACC) is a system of eastward flowing jets, standing meanders, and transient eddies that encircles Antarctica. It provides a pathway between the three major ocean basins, transmitting climate signals and smoothing out zonal differences in water properties (Rintoul

and Naveira Garabato 2013), and it plays an important role in global climate (Meredith et al. 2019). The steep isopycnals support the baroclinic flow of the ACC and inhibit the north–south exchange of heat and other properties. The ACC is also dynamically coupled to the Southern Ocean overturning circulation that makes a dominant contribution to the transfer of heat and carbon into the subsurface ocean (Frölicher et al. 2015; Armour et al. 2016).

The ACC is forced at the ocean surface by westerly winds and fluxes of heat and freshwater. A confounding feature of the ACC transport is its apparent insensitivity to changes in wind forcing. Observations and models consistently show that variability in the ACC's volume transport on time scales of

 Denotes content that is immediately available upon publication as open access.

Corresponding author: J. J. Meijer, janjaap.meijer@utas.edu.au

DOI: 10.1175/JPO-D-21-0049.1

© 2022 American Meteorological Society. For information regarding reuse of this content and general copyright information, consult the AMS Copyright Policy ([www.ametsoc.org/PUBSReuseLicenses](http://www.ametsoc.org/PUBSReuseLicenses)).

years to decades is small relative to the transport's mean value (Böning et al. 2008; Hogg et al. 2015), despite a 20% increase in wind stress over the past two decades (Rhein et al. 2013; Thompson et al. 2011). The insensitivity of ACC transport to wind forcing has been interpreted as evidence of “eddy saturation” of the current (Straub 1993) (the transport of the ACC is also constrained by the need to match the stratification in basins to the north; e.g., Gnanadesikan 1999). Eddy saturation refers to a limiting state in which increases in equatorward Ekman transport in response to stronger westerly winds are compensated by stronger poleward eddy fluxes, such that the slope of isopycnals (and hence the baroclinic transport of the ACC) does not change despite the increase in wind forcing.

While the essential role of baroclinic eddies in ACC dynamics is now clear from many modeling and observational studies (e.g., Olbers et al. 2004), recent work has emphasized the highly nonuniform distribution of eddy fluxes along the ACC (Naveira Garabato et al. 2011; Thompson and Sallée 2012). In altimetry (Fu et al. 2010; Foppert et al. 2017) and models (Hallberg and Gnanadesikan 2006; Meijers et al. 2007), eddy fluxes are found to be relatively weak along much of the circumpolar path of the ACC, and elevated downstream of major topographic features (e.g., Kerguelen Plateau, Southeast Indian Ridge/Macquarie Ridge, and Drake Passage). The elevated eddy fluxes downstream of topographic features are often associated with standing meanders of the ACC. However, detailed in situ observations of ACC standing meanders are rare and as a consequence the momentum and vorticity balances of standing meanders are not yet fully understood.

Thompson and Naveira Garabato (2014, hereafter TNG14) proposed a hypothesis to explain the role of standing meanders in the ACC. They suggested that over broad regions where the ACC flows with little interaction with topography, increased wind stress steepens isopycnals and accelerates the current. When the ACC interacts with topography, Rossby waves are generated and arrested by the flow to form a standing meander. The meander responds to increases in the upstream current speed by flexing (steepening), increasing the instability of the flow and the kinetic energy of transient eddies. The flexing of the meanders results in stronger downward transfer of momentum by internal stresses (interfacial form stress) that are proportional to cross-frontal buoyancy fluxes (Johnson and Bryden 1989). The downward momentum flux accelerates deep currents that can dissipate momentum through bottom form stress (Munk and Palmén 1951), the generation of internal waves (Nikurashin et al. 2013), or bottom friction. Bottom speeds greater than  $20 \text{ cm s}^{-1}$  are required in order for bottom friction to be significant (Gill 1968), which was previously thought to be unrealistically large. However, friction might contribute during energetic events such as those observed in the Subantarctic Front (SAF) southwest of Tasmania (peak speeds of  $29 \text{ cm s}^{-1}$  at 3500 dbar over periods of weeks; Meinen et al. 2002) and in Drake Passage, where near-bottom speeds of  $60\text{--}70 \text{ cm s}^{-1}$  lasting for 30–70 days were observed (Chereskin et al. 2009).

Processes well known in atmospheric science might provide a relevant analog for the meander flexing mechanism in the ocean. Meanders in the atmosphere have been studied

extensively for their role in the formation of midlatitude weather systems, and Newton (1959) was the first to connect these dynamics to meanders in the Gulf Stream. Cyclogenesis refers to the development of steep meander troughs coupled to the development of cyclones at depth (Savidge and Bane 1999b) by a mixed barotropic–baroclinic instability process in atmospheric and oceanic jets (Schubert et al. 2018). Divergence between troughs and crests and convergence between crests and troughs, driven by the ageostrophic component of the (gradient wind) flow field of the meander, cause a secondary vertical circulation along isopycnals. The divergence patterns between troughs and crests are also associated with shortening of the upper water column and stretching of the lower water column (Savidge and Bane 1999b). This connects the upper and lower water column, such that a horizontal circulation (cyclone) at depth can be associated with warm and cold advection that can release available potential energy. Additionally, these deep cyclones are associated with strong bottom currents, strong enough for bottom friction to become important and potentially enhance bottom form stress. While the process has received less attention in oceanography, cyclogenesis has been identified in observations and models of the Gulf Stream (Savidge and Bane 1999a,b; Schubert et al. 2018) and in observations of the ACC in Drake Passage (Chereskin et al. 2009).

To explore the dynamics of standing meanders in the ACC, we analyze a detailed survey of the velocity and water-mass properties within a standing meander of the SAF. We employ a gravest empirical mode (GEM) approach to construct a streamwise-average field against which to compare the evolution of temperature and salinity along the meander. Satellite altimeter observations are used with the gradient wind balance to estimate the geostrophic and ageostrophic velocity terms in the quasigeostrophic vorticity balance. This guides interpretation of along-stream water-mass changes and provides evidence that the process of cyclogenesis is at work during the time of the voyage. For the first time, we connect satellite altimetry data at the surface to subsurface water-mass changes in a standing meander in the ACC and relate the observed changes in water-mass characteristics to the dynamics of cyclogenesis.

Section 2 describes the in situ and satellite altimetry observations. Section 3 explains the construction of the GEM field and the decomposition used to distinguish between changes on isopycnals and changes due to vertical displacement of isopycnals. The approach used to estimate the surface velocity field and relevant terms in the gradient wind and vorticity balances is also discussed. Section 4 relates observed temperature anomalies on depth and density levels to the surface velocity and vorticity structure in the meander. In section 5, the different structure of temperature anomalies in the upper and lower water column is related to the quasigeostrophic vorticity balance and cyclogenesis. Section 6 synthesizes the conclusions of the study.

## 2. Data

### a. Subantarctic Zone Experiment (SAZE)

A standing meander in the SAF southwest of Tasmania was surveyed in March 1998 by the Research Vessel *Southern*

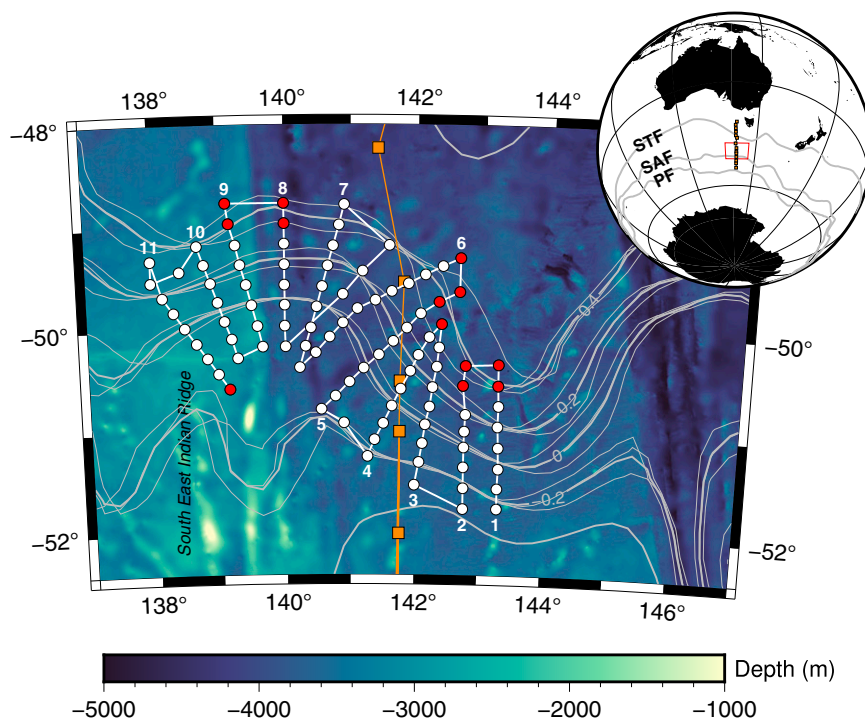


FIG. 1. Map of the study area. RV *Southern Surveyor* (white line) completed 11 transects (99 CTDs, circles) across a standing meander of the Subantarctic Front (SAF; white circles indicate stations used to define the along-stream average, see section 3). RSV *Aurora Australis* (orange line) collected CTD stations (orange squares) on the SR3 section crossing the meander from north to south. Bathymetry from [GEBCO Compilation Group \(2019\)](#) is shown in color contours. Gray contours indicate sea surface height [thick gray line is voyage time mean (12–28 Mar); thin gray lines are weekly means]. The inset shows the location of the study area, the SR3 transect (orange), the meander area (red box), and the mean positions of the Subtropical Front (STF, gray), the SAF (gray), and the Polar Front (PF, gray) from [Orsi et al. \(1995\)](#).

*Surveyor* voyage SS9802 to obtain a unique three-dimensional dataset of temperature, salinity, and velocity observations. The 99 CTD stations and shipboard ADCP (SADCP) observations were made along 11 hydrographic transects that crossed back and forth across about three quarters of a meander wavelength in the SAF near 50°S and 141°E (Fig. 1). The standing meander is a westward-propagating baroclinic Rossby wave, balanced by the eastward background current and initiated by the current flowing over the Southeast Indian Ridge following  $f/H$  contours. The CTD stations were spaced at approximately 12 n mi (22.2 km) in the cross-front direction and 18 n mi (33.3 km) in the alongfront direction and extend to ~1500-dbar depth. The SADCP measured at a frequency of 150 kHz with profiles limited to the upper 250–350 m, and the data were averaged in 8-dbar depth bins and averaged over 20-min time intervals. The sparse temporal and vertical resolution of the SADCP velocities made us decide to time-average over the period of the CTD cast and depth-average over the mixed layer depth. Mixed layer depth was determined with the temperature algorithm from [Holte and Talley \(2009\)](#). The data have been calibrated and quality controlled as described in the data processing reports available at [https://www.cmar.csiro.au/data/trawler/survey\\_details.cfm?survey=SS199802](https://www.cmar.csiro.au/data/trawler/survey_details.cfm?survey=SS199802).

During the same period, the Research and Supply Vessel (RSV) *Aurora Australis* surveyed along the repeated WOCE SR3 line at 140°E, to create a hydrographic transect that crossed from north to south straight through the meander survey (orange squares in Fig. 1). Data processing reports of this voyage are stored at [https://www.cmar.csiro.au/data/trawler/survey\\_details.cfm?survey=AU199706](https://www.cmar.csiro.au/data/trawler/survey_details.cfm?survey=AU199706).

#### b. Satellite altimetry

Satellite altimetry is used to calculate surface velocity and to provide spatial and temporal context for the ship measurements. The CNES-CLS13 mean dynamic topography (MDT, mean sea surface height over a consistent reference period from 1993 to 2012) is added to the Ssalto/Duacs gridded daily mean sea level anomaly (SLA) to obtain the absolute dynamic topography (ADT), from which geostrophic velocities are derived. The mean dynamic topography was produced by Collecte Localisation Satellites (CLS) Space Oceanography Division and the SLA, ADT, and geostrophic velocities are produced and distributed by the Copernicus Marine and Environment Monitoring Service (CMEMS), both available at <http://marine.copernicus.eu>.

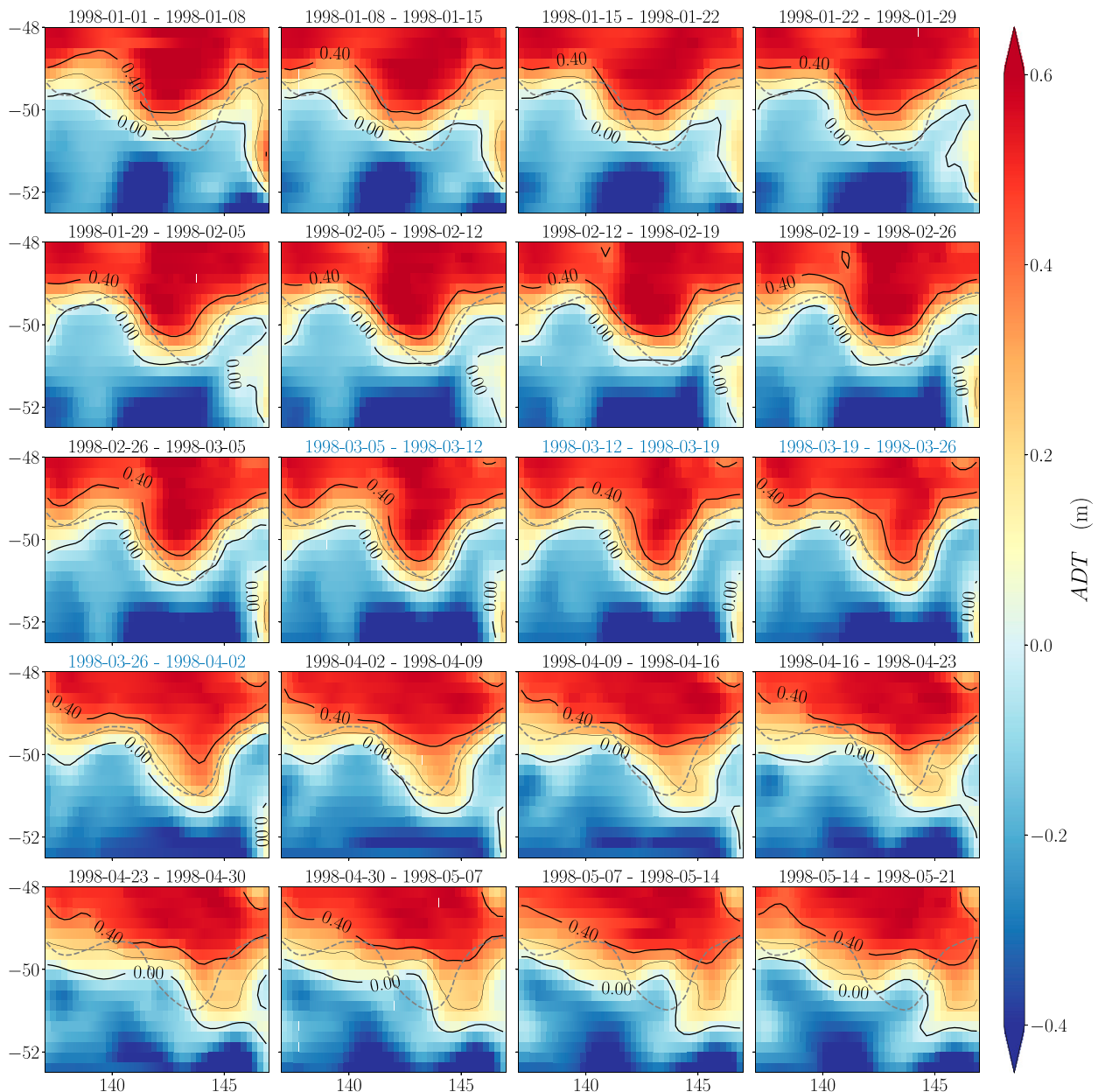


FIG. 2. Time evolution of the SAF meander with 7-day mean ADT contours from 1 Jan 1998 until 21 May 1998. The black ADT contours show the upper and lower limit of the front and a thin contour for the core of the front (0.2 m), the dashed gray line shows the core contour of the voyage time mean as a reference. The panels that were in the time period of the voyage (12–28 Mar 1998) have a title in blue.

We examined the evolution of the meander around our sampling time by showing 7-day averages of daily ADT maps (Fig. 2). In early January 1998, the ACC in our meander location had little curvature and progressively formed a meander during the rest of the month. From February to April, the meander grew in amplitude and curvature and translated slightly eastward. Steepest curvature was observed around the beginning of the voyage (12–28 March 1998), with a deep trough and crest. During this period the meander was fairly stable, but continued to translate slightly eastward. After the

voyage, the amplitude of the meander trough shrinks and the crest translated eastward returning to a near-zonal flow in May.

### 3. Methods

#### a. Gravest empirical mode fields

As shown in Figs. 3a and 3b, the Conservative Temperature and Absolute Salinity transects of the SR3 line have strong horizontal gradients associated with steepening of



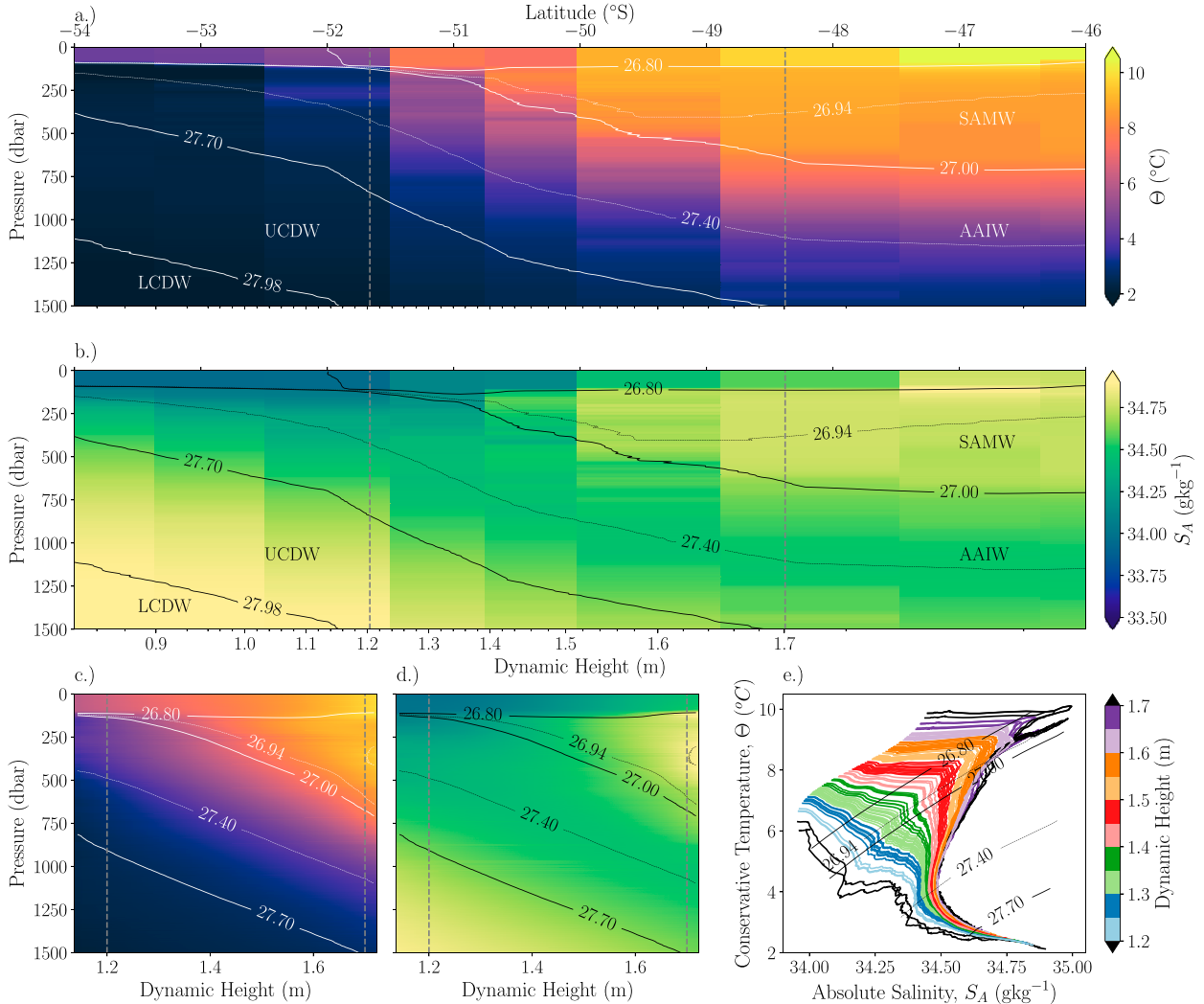


FIG. 3. Hydrographic properties during the meander survey. Sections from the SR3 line are shown: (a) Conservative Temperature  $\Theta(D, p)$  and (b) Absolute Salinity  $S_A(D, p)$ . Neutral density is shown in white/black contours. Dynamic height  $D(T, S, p)$  at 2 dbar relative to 1494 dbar is used as the primary  $x$  axis (bottom), and the corresponding latitude is shown at the top of each plot. Vertical dashed gray lines indicate the location of the standing meander. The two-dimensional GEM representation is shown: (c) Conservative Temperature  $\Theta(D, p)$  and (d) Absolute Salinity  $S_A(D, p)$  with contours of neutral density (white/black). (e) The GEM representation of the hydrography in a  $\Theta$ - $S_A$  diagram, with the color of each profile indicating the dynamic height  $D$ . Neutral density contours are shown in black.

the isopycnals in the SAF. Vertical gray dashed lines indicate the dynamic height band in which the standing meander was surveyed. We have divided the water column into water masses bounded by neutral density surfaces. The mixed layer (ML,  $\gamma_n < 26.8$ ) subducts to form Subantarctic Mode Water (SAMW,  $26.8 \leq \gamma_n < 27.0$ ) that then moves northward. The core of Antarctic Intermediate Water (AAIW,  $27.0 \leq \gamma_n < 27.7$ ), recognized by the salinity minimum, is close to the surface on the southern side of the front and around 1000 dbar on the northern side of the front (Rintoul and Bullister 1999; Sloyan and Rintoul 2001; Herraiz-Borreguero and Rintoul 2011). The colder and saltier layer below the AAIW is the Upper Circumpolar Deep Water (UCDW,  $27.7 \leq \gamma_n < 27.98$ ) from Orsi et al. (2002).

The ACC is characterized by deep-reaching density gradients that are associated with baroclinic jets extending throughout the water column. The subsurface gradients are reflected at the surface as gradients in ADT or dynamic height. Dynamic height has a strong relationship with the vertical structure of temperature and salinity, such that each dynamic height value is associated with a particular temperature and salinity profile over broad regions of the ACC. This has been exploited by previous studies to develop gravest empirical mode (GEM) climatologies of the Southern Ocean (e.g., Meinen and Watts 2000; Watts et al. 2001; Meijers et al. 2010).

Using this relationship, we create a two-dimensional GEM representation of the streamwise-average vertical temperature

and salinity structure of the meander from the hydrography observed in SAZE (Figs. 3c–e). A cubic spline function is fitted to the scatter of Conservative Temperature as a function of dynamic height  $D$  at each pressure level  $p$  for 86 of the 99 hydrographic stations to find the relationship  $\Theta(D, p)$ . The same approach is taken for Absolute Salinity to find  $S_A(D, p)$ . The dynamic height field is the height of the 2-dbar level relative to 1494 dbar, the deepest common level of all of the profiles. A few stations on the edge of the survey (red circles in Fig. 1) are outliers from this relationship and are excluded from the GEM. Along-stream anomalies in temperature and salinity are calculated by subtracting the GEM reference field from the observed field.

### b. Isopycnal property change and displacement

To identify the mechanisms responsible for water-mass evolution along the meander, we first decompose the temperature and salinity variability due to isopycnal property change from that due to isopycnal displacement (Bindoff and McDougall 1994). Property changes on isopycnals can arise from diapycnal mixing or along-isopycnal motion in the presence of along-isopycnal gradients of temperature and salinity (i.e., spiciness). Following the method of Bindoff and McDougall (1994), we use a Taylor decomposition to separate the isopycnal property change from the isopycnal displacement. The Taylor series to the first order is

$$\Theta'|_z = \Theta'|_\gamma - h'|_\gamma \frac{\partial \Theta^{\text{GEM}}}{\partial z} \Big|_\gamma, \quad (1)$$

where the prime indicates the anomaly of the observed field with respect to the GEM reference field [e.g.,  $\Theta'|_\gamma = \Theta(\gamma_n) - \Theta^{\text{GEM}}(\gamma_n)$  and  $h'|_\gamma = h(\gamma_n) - h^{\text{GEM}}(\gamma_n)$ ], and  $h$  is the depth of the neutral density layers in meters. The subscripts  $\gamma$  and  $z$  represent values on neutral density and depth surfaces, respectively.

To calculate the terms in Eq. (1), a few interpolations need to be made. The isopycnal property change (spice) term,  $\Theta'|_\gamma$ , is obtained by interpolating the Conservative Temperature from the pressure coordinate system to a regular interval neutral density coordinate system. For the isopycnal displacement (heave) term,  $h'(\partial \Theta^{\text{GEM}} / \partial z)|_\gamma$ , first the depth of the isopycnals,  $h$  and  $h^{\text{GEM}}$ , are interpolated on the regular interval neutral density coordinate system. Second, a nonregular depth coordinate system is created,  $z_m = (h + h^{\text{GEM}})/2$ , where the points in the coordinate system are the midpoints between the neutral density layers in the observed field and the GEM reference field (Bindoff and McDougall 1994). The vertical gradient of the Conservative Temperature in the GEM reference field and the Conservative Temperature anomalies on depth surfaces,  $\Theta'|_z$ , are interpolated to this  $z_m$  coordinate system, such that all temperature anomalies are on neutral density surfaces.

### c. Gradient wind balance

The strong curvature of the meander suggests that the centrifugal force needs to be taken into account and that the

meander flow is in gradient wind balance. From Holton (2004), the gradient wind balance is defined as

$$\kappa |\mathbf{u}|^2 + f |\mathbf{u}| = f |\mathbf{u}_g|, \quad (2)$$

where  $f$  is the Coriolis parameter,  $\kappa$  the curvature of the flow, and  $|\mathbf{u}|$  is the gradient wind velocity vector magnitude, which is a combination of geostrophic and ageostrophic components  $\mathbf{u} = (u, v) = (u_g, v_g) + (u_a, v_a) = \mathbf{u}_g + \mathbf{u}_a$ . Ageostrophic velocities are determined by subtracting the geostrophic velocities from the gradient wind velocities.

The gradient wind velocity is parallel to ADT ( $\eta$ ) contours. Geostrophic velocity is calculated from gradients in sea surface height (here we use the product provided by CMEMS) and the daily maps of ADT are used to calculate the curvature and gradient wind velocities. The curvature is calculated from the two-dimensional implicit curve defined by a function  $\eta(x, y) = 0$ :

$$\kappa \approx \kappa_g = \frac{-\frac{\partial^2 \eta}{\partial y^2} \left( \frac{\partial \eta}{\partial x} \right)^2 - \frac{\partial^2 \eta}{\partial x^2} \left( \frac{\partial \eta}{\partial y} \right)^2 + 2 \frac{\partial^2 \eta}{\partial x \partial y} \frac{\partial \eta}{\partial x} \frac{\partial \eta}{\partial y}}{\left[ \left( \frac{\partial \eta}{\partial x} \right)^2 + \left( \frac{\partial \eta}{\partial y} \right)^2 \right]^{3/2}}. \quad (3)$$

Solving Eq. (2) for the gradient wind velocity vector  $\mathbf{u}$  gives

$$\mathbf{u} = \frac{2\mathbf{u}_g}{1 + \sqrt{1 + 4\kappa_g |\mathbf{u}_g| / f}} \quad (4)$$

with the solution that gives  $\mathbf{u}(\kappa_g \rightarrow 0) = \mathbf{u}_g$  and a maximum total speed of  $|\mathbf{u}| = 2|\mathbf{u}_g|$ . The maximum speed is acquired when curvature dominates [ $\mathbf{u}_g = -f/(4\kappa_g)$ ] in Eq. (4). Since  $f$  is negative, and  $\mathbf{u}_g$  is positive in the trough and crest of an eastward flow,  $\kappa_g$  needs to be positive, which by convention means that the maximum speed can only occur in the crest of the meander. Note that a trough is on the equatorward side and a crest is on the poleward side of a meander, consistent with usage in the Northern Hemisphere.

### d. Quasigeostrophic vorticity balance

The meander we observed had a characteristic wavelength of roughly 500 km and an amplitude of about 165 km. The relative vorticity is small compared to the planetary vorticity and hence the quasigeostrophic assumption remains valid (see section 4d). The quasigeostrophic vorticity balance is

$$\frac{\partial \zeta}{\partial t} + \mathbf{u} \cdot \nabla \zeta + \beta v - f \frac{\partial w}{\partial z} = 0, \quad (5)$$

where  $\zeta = (\partial v / \partial x) - (\partial u / \partial y)$  is the relative vorticity calculated from the gradient wind velocities, and  $\beta = \partial f / \partial y$  is the meridional variation in Coriolis force. The first term in Eq. (5),  $\partial \zeta / \partial t$ , is the local rate of change of relative vorticity; the second term,  $\mathbf{u} \cdot \nabla \zeta$ , is the relative vorticity advection; the third term,  $\beta v$ , is the planetary vorticity advection; and the fourth term,  $-f(\partial w / \partial z)$ , is the vortex stretching. The vertical gradient of the vertical velocity is derived from the quasigeostrophic continuity equation as

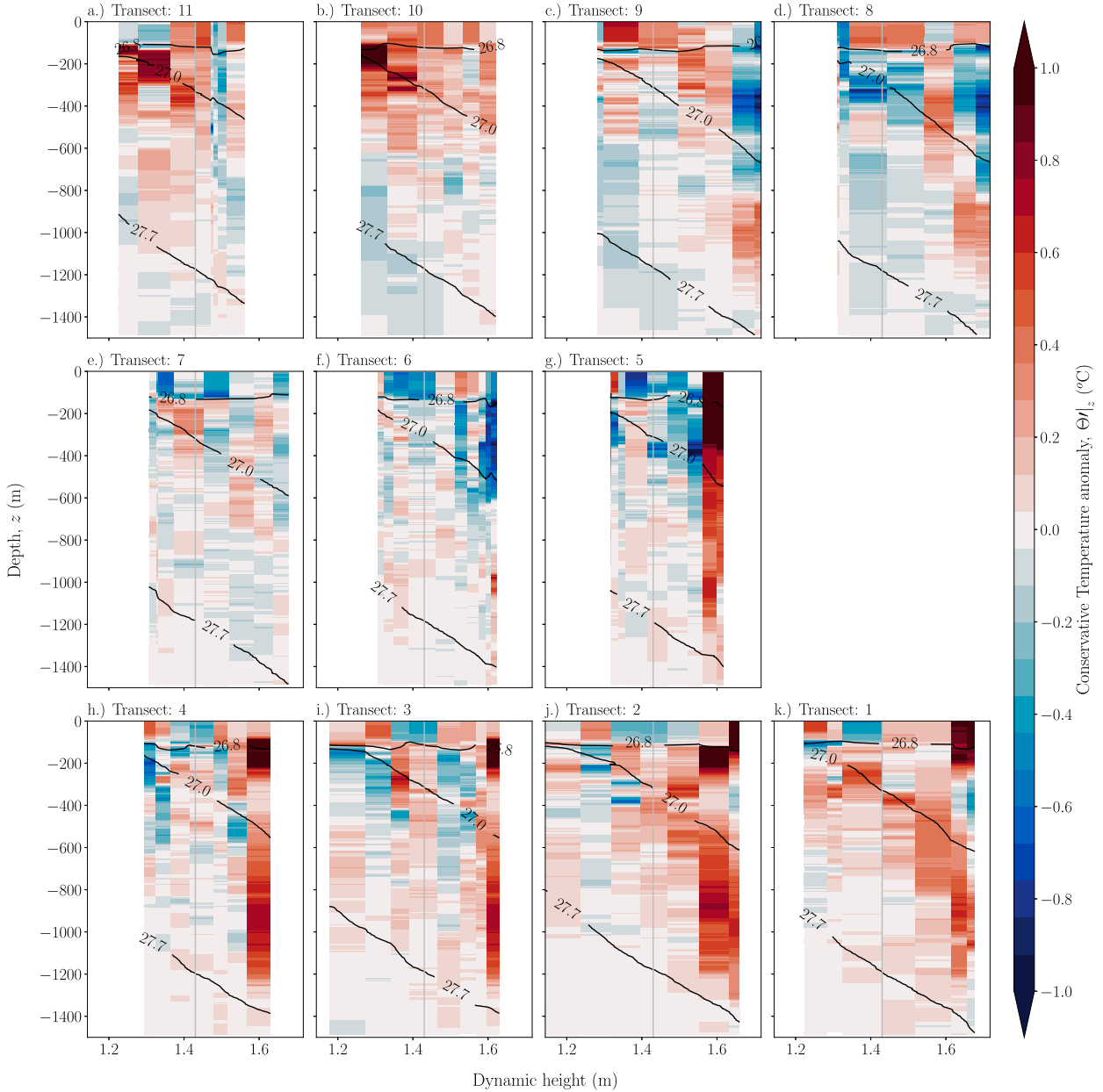


FIG. 4. Conservative Temperature anomaly from the two-dimensional GEM on depth levels for each transect. (top) Transects 8–11 are leading into the trough, (middle) transects 5–7 are in between trough and crest, and (bottom) transects 1–4 are leading into the crest. Neutral density contours bound the SAMW (26.8–27 kg m<sup>−3</sup>) and AAIW (27–27.7 kg m<sup>−3</sup>). The core of the front is indicated with a vertical gray line.

$$\frac{\partial w}{\partial z} = -\left(\frac{\partial u_a}{\partial x} + \frac{\partial v_a}{\partial y}\right) \quad (6)$$

and solely results from ageostrophic horizontal divergence. Calculating the curvature term in the gradient wind balance and the vorticity terms requires double differentiation, and errors are expected to increase with each level of differentiation, and therefore a single pass  $3 \times 3$  grid point boxcar smoother is applied after each differentiation as described by Hughes (2005).

## 4. Results

### a. Temperature anomalies on depth levels

Temperature anomalies with respect to the GEM reference field,  $\Theta'|_z$  (Fig. 4), show a distinct along-stream evolution in two broad layers: the upper part of the water column (150–600 m) and below 600 m. Water-mass changes in the surface mixed layer can be driven by air–sea interactions and are ignored here. This difference between upper and lower water column is particularly clear leading into the

trough (transects 11–8), where the anomalies change sign at about 600-m depth. The along-stream evolution is clear, the upper water column (150–600 m) is anomalously warm leading into the trough (Fig. 4, top row, transects 11–8), cooler in between trough and crest (middle row, transects 7–5), and then warms again going into the crest (bottom row, transects 4–1).

The deeper layer (>600 m) has a smaller signal, but there is a distinct pattern that can be discerned in the water-mass evolution from transect 11 to 1. The transects leading into the trough are anomalously cool at the lower dynamic heights ( $D < 1.6$ ), warmer in between trough and crest, and even warmer leading into the crest. This indicates a progressive warming along-stream in the deeper part of the water column. There are several profiles that are significantly warmer at higher dynamic height ( $D > 1.55$ ) in transects 9, 8, and 5–1. These are the profiles that were excluded from the GEM (section 3a). It is clear that there are different patterns of temperature anomalies in the upper and lower water column and the pattern of temperature change tends to follow the neutral density contours drawn to highlight the different water masses (Fig. 4). It therefore makes sense to use a neutral density as the vertical coordinate and the advantages that come from a density coordinate (e.g., Jackett and McDougall 1997).

#### b. Temperature anomalies on density levels

From the  $\Theta$ – $S_A$  diagram in Fig. 3e, we note that Conservative Temperature and Absolute Salinity increase on isopycnals with increasing dynamic height (i.e., water is warmer and saltier to the north on all isopycnals above the CDW). The temperature changes in Fig. 4 are separated into temperature changes on isopycnals (spice, Fig. 5) and changes due to isopycnal displacement (heave, figure not shown), by means of Eq. (1). As explained in section 3b all temperature changes in Eq. (1) are interpolated on density surfaces, which allows us to compare temperature changes on isopycnals and caused by isopycnals displacement to temperature changes on depth levels at midpoints,  $z_m$ . Temperature changes on isopycnals over all depths of the CTD profiles ~1500 dbar are significantly larger ( $R^2 = 0.88$ ) than those caused by displacement of isopycnals ( $R^2 = 0.10$ ). This is an unusual result in the context of earlier work Bindoff and McDougall (2000), where temperature changes caused by heave are typically larger than the changes of temperature on isopycnals.

The isopycnal layers corresponding to SAMW and upper AAIW are anomalously warm leading into the trough (transects 11–8, Figs. 5a–d), become progressively cooler between the trough and the crest (transects 7–5, Figs. 5e–g) and become warmer again entering the crest (transects 4–1, Figs. 5h–k). Thus, in an along-stream sense, these upper layers are cooling on the upstream side of the meander and warming through the downstream side. The deeper isopycnal layers corresponding to denser AAIW and UCDW are anomalously cool leading into the trough, become warmer in between trough and crest, and even warmer leading into the crest.

A clearer picture of the along-stream evolution of temperature anomalies can be gained by averaging in density layers and between streamlines, as discussed in section 5. The difference between the along-stream evolution of temperature anomalies in the upper and lower water column suggests they may be controlled by different processes. Note that by definition, temperature change on a neutral surface is accompanied by a density-compensating change in salinity  $S'_A|_\gamma$ . The spatial pattern of salinity anomalies (not shown) therefore mirrors those shown for temperature (Fig. 5).

#### c. Velocity structure

We next seek to relate the along-stream evolution of the temperature anomalies to the dynamics of the meander. Figure 6a shows the velocity field estimated from ADT with the SADC velocity vectors overlaid. The close correspondence between the SADC and gradient wind estimates of total velocity provides confidence that the gradient wind velocities calculated from satellite data are realistic (the correlation between the magnitude of the SADC and gradient wind velocities is  $R^2 = 0.53$  and between the SADC velocity direction and the orientation of the ADT contours is  $R^2 = 0.49$ ). The SADC velocity is weaker in the trough and stronger in the crest, consistent with the ageostrophic flows diagnosed using the gradient wind balance (Fig. 6b). The colors in Fig. 6b show the relative importance of curvature and rotation effects on the flow, represented by the ratio of the ageostrophic and total velocity,  $u_a/|u|$ . This ratio is analogous to the Rossby number,  $Ro$ , as can be seen by taking the radius of curvature,  $R = 1/\kappa$ , as the characteristic length scale  $L$ , the velocity scale as  $U = U_g + U_a$ , and substituting  $Ro = U/Lf$  in the gradient wind balance to show  $Ro \sim (U_a/U)$ .

Recall that the ageostrophic and geostrophic velocity vectors are parallel, as we are considering ageostrophic flow due to curvature changes, not friction (i.e., Ekman spiral). The geostrophic flow speed increases in the extremes (trough/crest) of the meander associated with enhanced ADT gradient from meander steepening. The total flow speed is decelerated in the trough and accelerated in the crest by the ageostrophic velocity (Fig. 6b), creating the conditions for divergence of the flow field. This divergence is in contrast to a geostrophic flow field, which is by definition divergence free. The colors in Fig. 6b show the relative importance of curvature against rotational effects on the flow (or Rossby number), represented by the relative contribution of the ageostrophic to the total flow speed. From a momentum balance perspective these differences in flow speed are explained by the centrifugal force being in the opposite direction to the pressure gradient force in the trough and in the same direction in the crest. Hence, the ageostrophic flow opposes the geostrophic flow in the trough, and reinforces the geostrophic flow in the crest, resulting in a divergent total flow field.

#### d. Vorticity budget

##### 1) TOPOGRAPHIC STEERING AND RELATIVE VORTICITY

Conservation of barotropic potential vorticity implies that



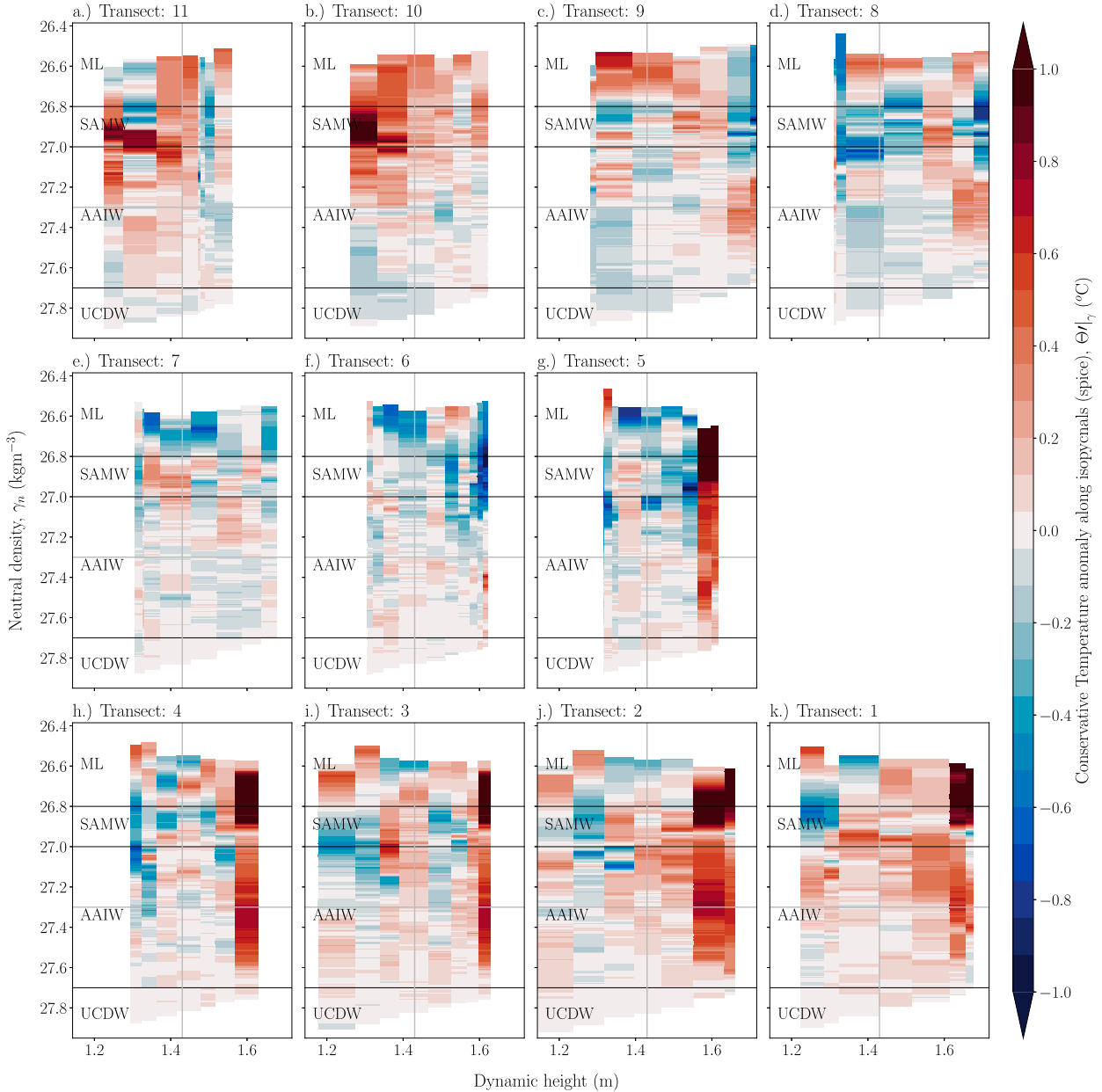


FIG. 5. Conservative Temperature anomaly on neutral density levels due to isopycnal property changes, for each transect. Neutral density layers bounding the different water masses [mixed layer (ML), Subantarctic Mode Water (SAMW), Antarctic Intermediate Water (AAIW), and Upper Circumpolar Deep Water (UCDW)] are indicated by the horizontal black lines. The core of the front and the separation between the upper and lower water column are indicated with gray lines.

$$\frac{\zeta + f}{H} = \text{constant}. \quad (7)$$

The flow will therefore tend to follow  $f/H$  contours, where relative vorticity  $\zeta$  is small compared to the planetary vorticity  $f$ ,  $H$  is the depth of the water column. Upstream of the meander ( $137^\circ$ – $139.5^\circ\text{E}$ ), the flow is steered to the north over shoaling topography, creating negative relative vorticity (Fig. 7). Between  $139.5^\circ$  and  $141.5^\circ\text{E}$ , the topography rapidly deepens. The rapid change in depth causes stretching of the

water column and generates stronger relative vorticity. From  $141.5^\circ$  to  $143^\circ\text{E}$ , the sea floor is relatively flat. To conserve potential vorticity there must therefore be an increase in planetary vorticity, hence poleward flow (Fig. 7b). Leading into the crest (from  $143^\circ$  to  $145^\circ\text{E}$ ), the flow starts following  $f/H$  contours again, before it makes another jump into deeper water, which creates another trough in the same way as described above. The trough/crest are clearly areas of negative/positive relative vorticity (Fig. 7b). Although relative vorticity is much smaller than the planetary vorticity, the difference in planetary vorticity between

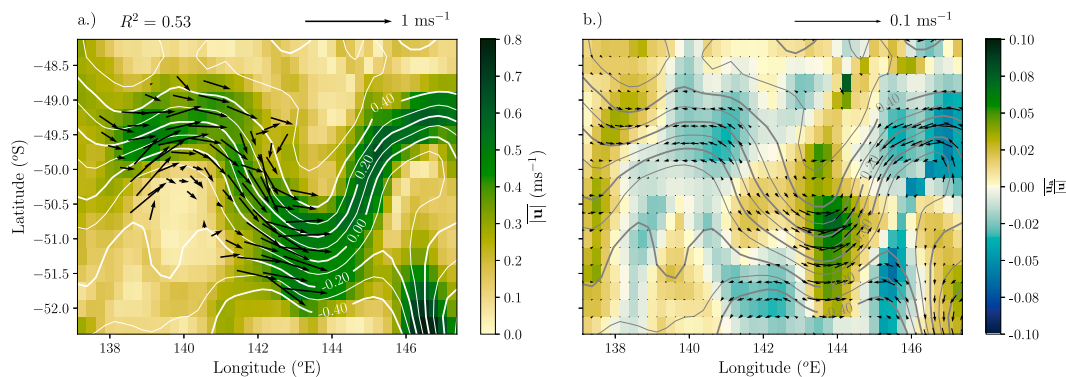


FIG. 6. (a) Time-mean (indicated with an overbar) surface flow speed over the period of the voyage in color, derived from the gradient wind balance and satellite altimetry derived variables [absolute dynamic topography (ADT) and geostrophic velocities]. On top are drawn the voyage time-mean ADT contours (white) and the SADCPC absolute velocities averaged over the mixed layer depth and over the time period of each CTD cast (black arrows). The correlation coefficient between SADCPC absolute velocities and the gradient wind velocities (interpolated to the location of the CTD cast) is noted at the top of the panel, where the gradient wind vectors are derived from the satellite altimetry data nearest time. (b) The ratio between the ageostrophic and total (gradient wind) flow speed (in color), which is similar to the Rossby number  $Ro \sim u_a/|u| = (|u| - |u_g|)/|u|$  overlaid with the voyage time-mean ADT contours (gray) and the ageostrophic velocity vectors (black arrows).

trough and crest is comparable to the difference in relative vorticity. An otherwise simple gradient in Coriolis parameter between north and south is modulated by relative vorticity that clearly shows a meander in the absolute vorticity (Fig. 7c). The

quasigeostrophic assumption remains largely valid (Fig. 7d), but becomes critical ( $\zeta/f \geq 0.1$ ), in the crest at  $144^\circ\text{E}$  and the trough at  $146^\circ\text{E}$  where the ageostrophic components of the flow becomes significant [ $|u_a| \geq \mathcal{O}(0.1)$ , Fig. 6b].

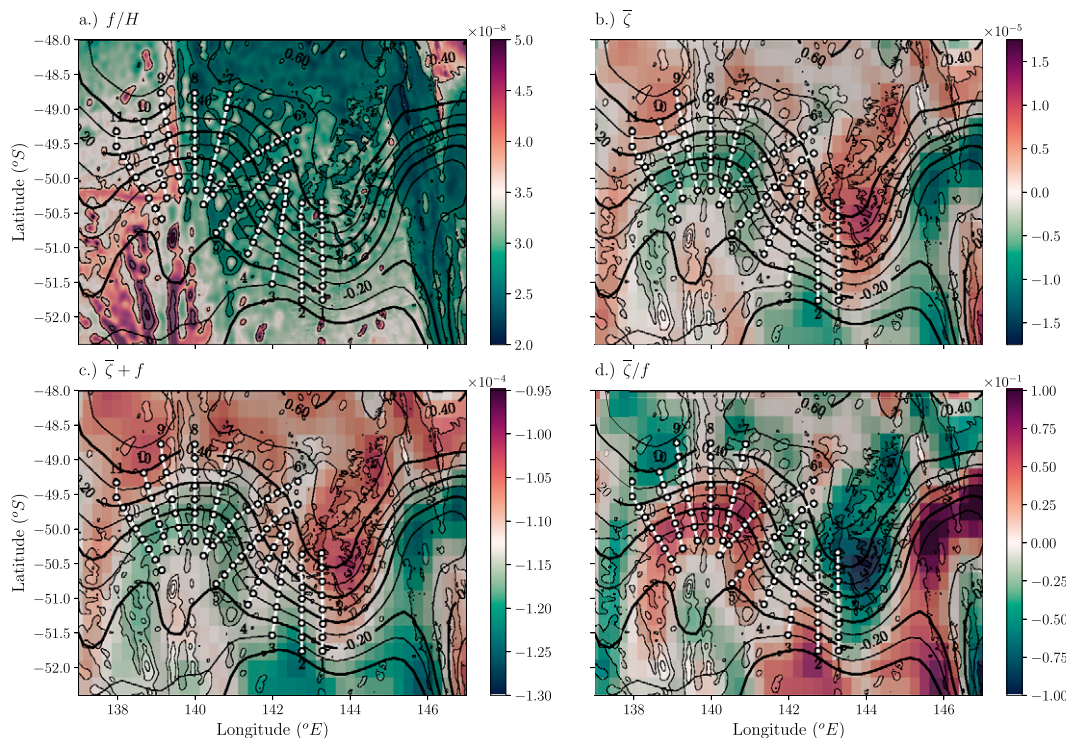


FIG. 7. Terms in the barotropic potential vorticity equation: (a) topographic steering is indicated by  $f/H$  contours ( $\text{m}^{-1} \text{s}^{-1}$ ), (b) the time-mean relative vorticity  $\bar{\zeta}$  ( $\text{s}^{-1}$ ), (c) the time-mean absolute vorticity  $\bar{\zeta} + f$  ( $\text{s}^{-1}$ ). (d)  $\bar{\zeta}/f$  contours are drawn to evaluate where the quasigeostrophic assumption remains valid ( $\bar{\zeta}/f \ll 1$ ). Bathymetry contours are shown in gray shading in the background, the voyage time-mean ADT contours are shown in black, and the hydrographic stations and transects are plotted by the white connected dots.

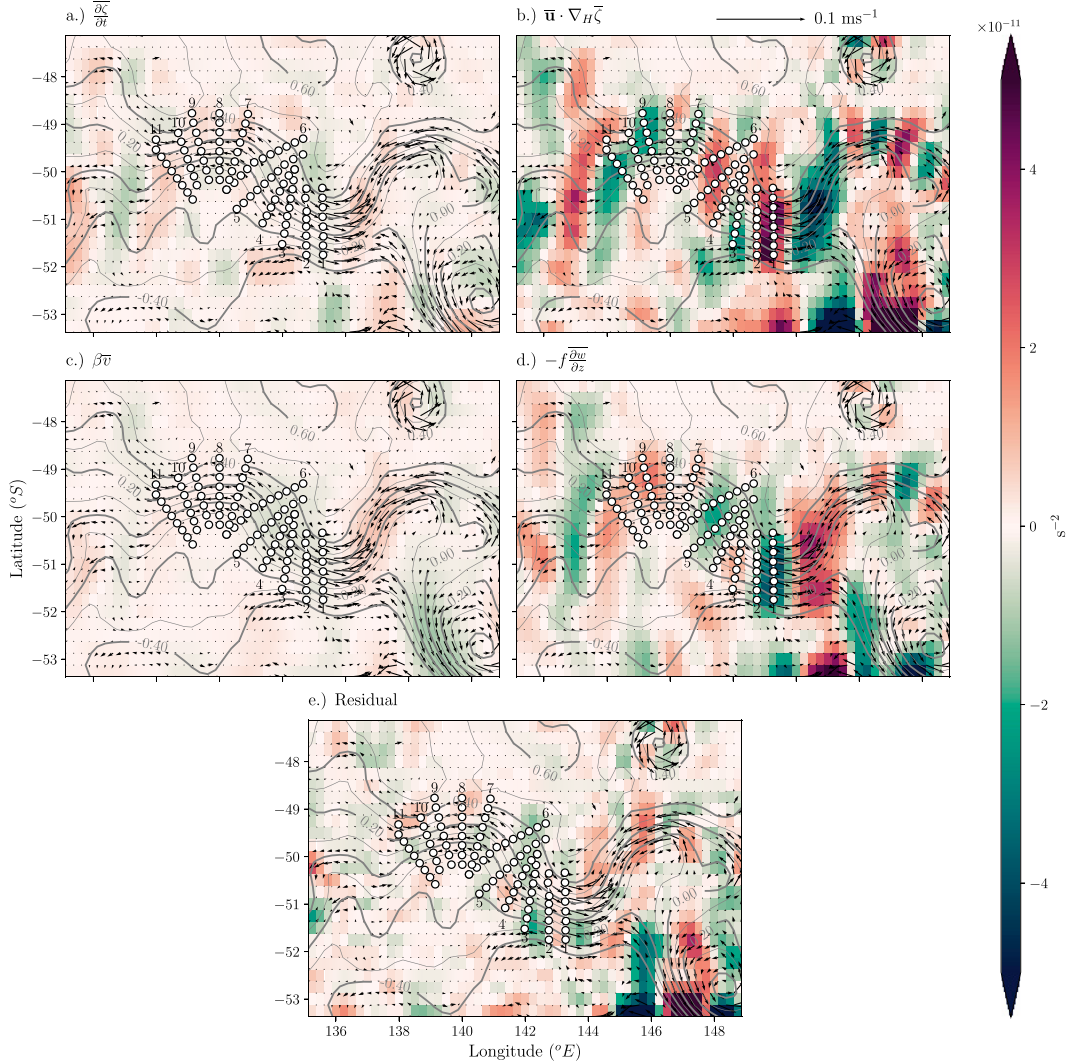


FIG. 8. Terms of the quasigeostrophic vorticity balance: (a) local time derivative of relative vorticity  $\partial\zeta/\partial t$  ( $\text{s}^{-2}$ ), (b) the advection of relative vorticity  $\mathbf{u} \cdot \nabla_H \zeta$  ( $\text{s}^{-2}$ ), (c) the advection of planetary vorticity  $\beta\bar{v}$  ( $\text{s}^{-2}$ ), (d) the vortex stretching (convergence is shown in red and divergence in green)  $-f(\partial w/\partial z)$  ( $\text{s}^{-2}$ ), and (e) the residual, which is the sum of the three terms in (a)–(d) ( $\text{s}^{-2}$ ). The voyage time-mean ADT contours are shown in gray, the ageostrophic velocity vectors are indicated with black arrows and the hydrographic stations and transects are plotted by the white connected dots.

## 2) QUASIGEOSTROPHIC VORTICITY BALANCE

The time-mean individual terms of the quasigeostrophic vorticity equation [Eq. (5)] over the voyage duration are shown in Fig. 8. From the panels we see that the first-order balance is between the advection of relative vorticity (Fig. 8b) and the vortex stretching (Fig. 8d) within the meander area ( $R^2 = 0.87$  interpolated to the CTD locations). Leading into the trough, the negative relative vorticity advection (Fig. 8b) is associated with convergence of the streamlines and vortex stretching (Fig. 8d), which is also shown by the ageostrophic velocity vectors (black arrows in all panels) and suggests downwelling in transects 8–11. In between trough and crest, where barotropic relative vorticity is nearly zero (Fig. 7b), the

advection of relative vorticity (Fig. 8b) is positive (transects 5–6), causing divergence and upwelling. The ageostrophic velocity vectors in Fig. 8 show the convergence/divergence, which we infer to be downwelling/upwelling areas. The ADT contours converge in the crest causing the strong advection of relative vorticity (note that strongest advection of relative vorticity in a pure sinusoidal wave would be expected in the middle between trough and crest, and crest and trough). Also, a filament interacting on the poleward side of the crest contributes to the strong advection of relative vorticity in the crest (52°S, 142°E). The local time derivative of relative vorticity (Fig. 8a) and the advection of planetary vorticity (Fig. 8c) are about an order of magnitude smaller than the

relative vorticity advection and the vortex stretching terms. The residual (Fig. 8e) is small in the area of the observations and reflects the major balance is between the relative vorticity advection and the vortex stretching. East of 144°E, where the quasigeostrophic assumption breaks down ( $\zeta/f \sim 0.1$ ) the residual is of the same order of magnitude as the two dominant terms. The residual is a combination of the generation of vorticity by the wind stress curl and the dissipation of vorticity by bottom pressure torque. It potentially includes the vortex tilting too, which becomes important in the growth and decay of baroclinic Rossby waves (Holton 2004).

## 5. Discussion

Using a detailed survey of a standing meander, we investigated the evolution of temperature anomalies along the meander for the signature of the dynamical processes at work.

### a. Observed temperature changes

Previous work has found a clear signal of warming due to both displacement of isopycnals (heave) and warming on isopycnals (spice) across most depth levels in the Southern Ocean (e.g., Meijers et al. 2011, their Fig. 7 and Table 1), with the larger component caused by the heave or “adiabatic” component. Firing et al. (2017) showed that 95% of the deep ( $>2000$  m) temperature variability of repeated sections in the Drake Passage is explained by heave in the Polar Front and Subantarctic Front. In sharp contrast, we find that in the standing meander of our survey, changes in water-mass properties on isopycnals dominate and explain 88% of the temperature variability on depth levels and only 10% of the variability is explained by isopycnal displacement. This contrast may be because our study is focused on a standing meander during a period of growth, so the along-isopycnal changes driven by divergence/convergence are relatively large. Other studies (e.g., Meijers et al. 2011) examine larger regions that incorporate areas away from topography and standing meanders with more zonal flows and dynamically quiet regions between fronts, where ageostrophic divergence is small.

In Fig. 9, we summarize the along-stream changes in temperature. Figure 9a shows the average temperature anomaly at each transect averaged over the dynamic height range spanning the meander ( $1.32 \leq D < 1.55$ ), as a function of density. Figure 9b presents the surface integral of the temperature anomalies on isopycnals over two density layers ( $\gamma_n$  26.8–27.3 representing the SAMW and upper AAIW, and  $\gamma_n$  27.3–27.7, representing the lower AAIW) and over the same dynamic height range ( $A = \iint \Theta' d\gamma dD$ ). In the upper density layer, warm anomalies relative to the background GEM occur leading into the trough (transects 11–9, Figs. 9a,b), cool anomalies occur exiting the trough (transects 8–3), and warm anomalies are again present entering the crest (transects 2–1). There is along-stream cooling leading into the trough (transect 10–6) and along-stream warming entering the crest (transect 5–1). In the lower water column ( $\gamma_n > 27.3$ ), anomalously cold water in the trough (transects 7–10, Figs. 9a,b) becomes progressively warmer moving into the crest (transects 1–4). The surface integrated temperature anomaly in the lower water

column (Fig. 9b, blue line) contributes only a small amount to the integrated anomaly over the whole water column (gray line). However, it reveals a robust pattern of warming from trough to crest that is less affected by the strong variability in the upper water column.

In the following sections we discuss the dynamics that explain the along-stream evolution of temperature anomalies in the upper (section 5b) and lower water column (section 5c) and the evidence for cyclogenesis at the time of the survey (section 5d).

### b. Water-mass evolution in the upper water column

In meanders where the curvature is large, the geostrophic balance no longer holds: the introduction of the centrifugal force in the cross-stream momentum balance (gradient wind balance) causes an asymmetry in the flow field between troughs and crests. Through mass conservation, this leads to patterns of horizontal divergence. In the atmosphere, for example, divergence in the upper troposphere is connected to convergence at the surface, leading to rising air masses, condensation, and precipitation (Palmén and Newton 1969).

Bower (1989) shows patterns of horizontal divergence from float observations ( $\sim 400$ – $800$  dbar) in Gulf Stream meanders and describes divergence upstream of crests and convergence upstream of troughs. A similar pattern is found in the SAF meander: the ageostrophic flow decelerates the current in the trough and accelerates it in the crest (Fig. 6b), causing divergence between the trough and the crest and convergence between the crest and the trough (Fig. 8b).

TNG14 and Firing et al. (2016) point out the importance of the ageostrophic velocities in the vorticity budget of standing meanders in the ACC. The ageostrophic contribution to the total velocity might be small, but the spatial variability is significant for the divergence of the velocity field and the relative vorticity gradients. Hughes (2005) calculated the terms in the steady barotropic vorticity balance and assumed the divergence term to be small. They concluded that the relative vorticity advection is balanced by the advection of planetary vorticity ( $\beta v$ ). This result largely holds outside of the large meander areas (TNG14). However, TNG14 show in a high-resolution, eddy-resolving ocean GCM that in meander regions the planetary vorticity term is an order of magnitude smaller than the other terms and that the dominant balance is between vortex stretching and advection of relative vorticity. Firing et al. (2016) confirm this first-order balance with full-depth observations in the Drake Passage and found that the surface vorticity advection is a sufficient representation of the depth-integrated vorticity balance. In our study of an ACC standing meander, we also confirm with satellite observations that advection of relative vorticity is balanced by vortex stretching/divergence (Figs. 8b,d) and that the advection of planetary vorticity is about an order of magnitude smaller (Fig. 8c). At the locations of the CTDs in this experiment we found that 87% of the variability in the quasigeostrophic vorticity balance is explained by relative vorticity and vortex stretching.



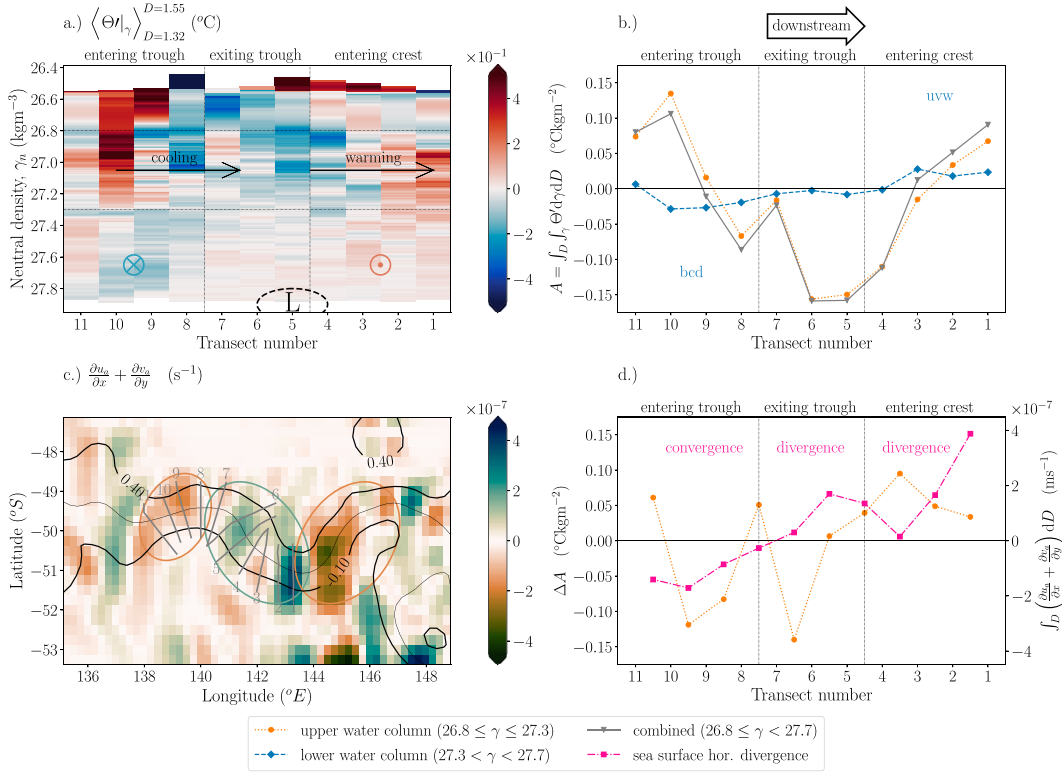


FIG. 9. Summary of the Conservative Temperature anomalies on isopycnals in Fig. 5 with (a) a side view from south to north averaged within the range of dynamic heights common to all transects ( $1.32 \leq D < 1.55$ ) and (b) by calculating the surface integral  $A$  of the temperature anomaly over the upper ( $26.8 < \gamma \leq 27.3$ ), lower ( $27.3 \leq \gamma < 27.7$ ), and combined ( $26.8 \leq \gamma < 27.7$ ) water columns in the same dynamic height range. The mnemonic bed refers to backing, cold advection, and downwelling, and uvw refers to upwelling, veering, and warm advection (Lindstrom et al. 1997). (c) A plan view of the SAF meander (Fig. 1) with convergence (orange ellipse)/divergence (green ellipse) patterns and the voyage averaged sea surface height contours in black. (d) Combines the first difference of the surface integral in (b),  $\Delta A$  between transects, with overlaid the integral of surface velocity divergence over the same dynamic height range at each transect, averaged between adjacent transects (pink). In the upper water column convergence at the surface is collocated with along-stream cooling suggesting downwelling of cooler water and divergence is collocated with along-stream warming suggesting upwelling of warmer water. In (a), the blue/red vectors perpendicular to the figure plane show the turning of the velocity vector with depth in the lower water column. They indicate cross-frontal transport by the hypothesized cyclogenesis process linked to the surface divergence/upwelling, speeding up bottom currents.

Any baroclinic flow that is not entirely geostrophic must have some form of vertical motion as a consequence of continuity [Eq. (6)]. In Fig. 9c, we link the upper water column temperature changes to the surface divergence patterns from altimetry. Figure 9d presents the first difference of temperature change in the upper water column to indicate the along-stream warming/cooling (from Fig. 9b) overlaid with the cross-stream integral of divergence for each transect (from Fig. 9c). In the upper water column ( $26.8 < \gamma \leq 27.3$ ), our observations reveal convergence entering the trough (Figs. 9c,d), vortex stretching ( $\partial w / \partial z > 0$ ; Fig. 8d) and warm anomalies on isopycnals (Fig. 9a) that progressively cool from transect 10 to transect 6 (Fig. 9d). Exiting the trough and entering the crest, divergence, vortex squeezing and cold anomalies (that progressively warm from transect 6 to transect 1) are present. We infer that the convergence entering

the trough is associated with downwelling of cooler water along isopycnals and the divergence exiting the trough and entering the crest is associated with upwelling of warmer water along isopycnals. (Recall from Fig. 3e that temperature and salinity decrease with decreasing dynamic height, i.e., to the south, along isopycnals.) The anomalies relative to the GEM of isopycnal height ( $h'$ , not shown) suggest vortex stretching (and squeezing) associated with convergence and divergence [Eq. (6)]. Entering the trough (transects 11 and 10) we observe a thickening of the SAMW and upper AAIW and a thinning of SAMW and upper AAIW between trough and crest (transects 6 and 5) that is consistent with this view. Entering the crest (transects 3–1) we see a thickening of isopycnal layers again, which is consistent with the warm temperature anomaly, but unexpected regarding the strong divergence at the surface. The divergence (or vortex squeezing) seen in the



quasigeostrophic vorticity term is attributed to the particularly strong curvature in the meander here and is enhanced due to encroachment of another front from the south.

*c. Nonequivalent barotropic flow and cross-front transport in the lower water column*

In the Synoptic Ocean Prediction (SYNOP) Experiment in the Gulf Stream, [Savidge and Bane \(1999a,b\)](#) show how deep cyclonic circulation patterns are formed under standing meander troughs and how this coincides with patterns of divergence at the surface and convergence at depth. These cyclones were present 35% of the time with strong bottom speeds of up to  $0.5 \text{ m s}^{-1}$ . This observed divergence and convergence in the water column is analogous to atmospheric cyclogenesis and has been simulated by [Schubert et al. \(2018\)](#) in a high-resolution ocean general circulation model. It shows the connection between meander troughs at the surface and benthic storms at the bottom.

[Hughes \(1995\)](#) argues that when the background current is much faster than the wave speed as found in the ACC, the flow approximates an equivalent-barotropic structure, where the surface current is parallel to the current at depth. However, there have been several studies of standing meanders in the Gulf Stream ([Lindstrom et al. 1997](#)) and in the Antarctic Circumpolar Current ([Phillips and Bindoff 2014](#); [Watts et al. 2016](#)) that show a nonequivalent barotropic flow. [Lindstrom et al. \(1997\)](#), in the SYNOP experiment, found a backing of the horizontal flow (cyclonic rotation from deep to shallow levels), cold advection, and downwelling entering a meander trough or exiting a crest, and veering, warm advection, and upwelling exiting a trough or entering a crest. They gave these patterns the mnemonics “bcd” and “uvw.” [Phillips and Rintoul \(2000\)](#) and [Tracey et al. \(2006\)](#) found that this result for Gulf Stream meanders also held for the SAF south of Australia. [Phillips and Bindoff \(2014\)](#) observed similar patterns of upwelling and downwelling phase-locked with a meander at the northern Kerguelen Plateau, associated with the nonequivalent barotropic flow.

In this study, the temperature anomalies in the lower water column ([Fig. 5](#)) can be explained by the relationships identified in [Lindstrom et al. \(1997\)](#). Entering the trough (transects 8–10, [Fig. 9a](#)), we expect to see cyclonic (clockwise) rotation of the horizontal velocity vector from deep to shallow (backing), transporting colder, fresher water down slope to the north along isopycnals, and downwelling. Leading into the crest (transects 1–4), we expect to see anticyclonic rotation from deep to shallow (veering, anticlockwise), transporting warmer and saltier water up slope to the south along isopycnals, and upwelling. These patterns are entirely consistent with the relatively cold anomalies leading into the trough and relatively warm anomalies entering the crest ([Fig. 9](#)). The net effect is that colder water crosses dynamic height contours leading into the trough, moving equatorward, and warmer water crosses dynamic height contours between the trough and the crest, moving poleward at depth. This indicates a net poleward heat transport.

*d. Potential impacts of cyclogenesis on bottom processes and momentum dissipation*

The difference in temperature anomaly patterns between the upper and the lower water column strongly suggest that the shipboard survey was undertaken during a cyclogenesis event. Cyclogenesis is a term adopted from meteorology and describes how Rossby waves (wavelike motion) in the midlatitude jet stream are connected to high and low pressures (circular motion) at the surface. In a similar way standing meanders at the surface can be connected to low (and high) pressures at the ocean bottom. In [Fig. 9c](#), an approximately stationary Rossby wave at the sea surface causes patterns of divergence and convergence due to the ageostrophic contributions in the flow. Through conservation of mass, this must lead to patterns of up- and downwelling, respectively, leading to the temperature anomalies in the upper water column. This is sometimes referred to as vertical secondary circulation. Convergence at the surface is collocated with a subsurface cooling suggesting downwelling entering the trough. Divergence is collocated with a warming, suggesting upwelling exiting the trough and entering the crest. In the lower water column this leads to cold advection leading into the trough and warm advection leading into the crest, creating a horizontal circulation. The vertical limit of the CTD profiles to  $\sim 1500$  dbar did not allow us to quantify the temperature anomalies near the bottom, but considering the observations by [Savidge and Bane \(1999a,b\)](#) and model experiments by [Schubert et al. \(2018\)](#) of meanders in the Gulf Stream, it is quite likely that a deep cyclone, i.e., benthic storm, is present between the trough and crest during this survey ([Fig. 9a](#)).

Furthermore, the fact that the temperature anomalies on isopycnals in the lower water column are about a quarter wavelength out of phase from the upper water column anomalies ([Fig. 9b](#)) indicates potential growth of the baroclinic Rossby wave. This phase offset is evident in [Fig. 9](#), where the minimum temperature anomaly in the lower water column in transect 6 is offset by about a quarter wavelength from the maximum temperature anomaly in the upper water column in transects 1 and 10. As explained in [Cushman-Roisin and Beckers \(2011\)](#), a quarter wavelength between the surface and the deep Rossby wave (in an idealized two-layer model) is the most favorable condition for initial growth of baroclinic instability. Based on the observations in the lower water column, the deep cyclone center is expected between the trough and crest (transects 5–6), where the temperature anomalies are approximately zero ( $A \sim 0$ ), between maxima in the trough (transect 10) and crest (transect 1). This suggests that the system is in its initial to middle stage of cyclogenesis, consistent with steepening of the meander during the survey ([Fig. 2](#)). In the mature stage of the instability, the cyclone would be collocated with the trough.

The theory of cyclogenesis has important implications for our understanding of meanders in the ACC. Deep cyclones can speed up bottom currents, which in turn can increase bottom form stress, generate lee waves over rough topography and increase bottom friction that leads to the dissipation of momentum. This might be an explanation for how standing

meanders remove the additional momentum added to the ACC by accelerating Southern Ocean westerlies, as proposed by TNG14, allowing the ACC's volume transport to remain steady. Moreover, the nonequivalent barotropic flow within the meander causes along-isopycnal cold advection equatorward leading into the trough and warm advection poleward leading into the crest. The result is enhanced poleward advection of heat in standing meanders as identified in many recent studies, (e.g., Naveira Garabato et al. 2011; Watts et al. 2016; Foppert et al. 2017).

## 6. Conclusions

By constructing a streamwise-average temperature and salinity GEM field from 99 hydrographic stations, anomalies were calculated along 11 transects in the survey of a Subantarctic Front standing meander. We found that the anomalies were mainly due to water-mass changes on isopycnals, rather than due to heaving. This is contrary to a range of other studies in the Southern Ocean that find the heave component dominates temperature changes in the ACC (e.g., Meijers et al. 2011; Firing et al. 2017). The upper and lower water column showed different patterns of temperature (and salinity) variation along the front. In the upper water column ( $\gamma_n < 27.3$ ), anomalously warm water on isopycnals leading into the trough became progressively cooler and then warmer again leading into the crest. In the lower water column, cold anomalies were observed in the trough, becoming progressively warmer in between trough and crest and warmest in the crest.

Using the gradient wind balance, the total horizontal velocity (geostrophic + ageostrophic) at the surface was calculated from satellite altimetry observations. In this meander, generated by the ACC flowing over strongly varying topography, the curvature of the flow causes patterns of divergence and convergence. Divergence is due to the ageostrophic contribution to the flow, decelerating the current in the trough and accelerating it in the crest. This is in contrast to areas outside meander regions where the flow has weak curvature and the ageostrophic term is negligible (Rintoul and Naveira Garabato 2013).

We calculated terms in the steady quasigeostrophic vorticity balance and showed that the major balance is between advection of relative vorticity and vortex stretching. Convergence between crests and troughs and divergence between troughs and crests implies areas of downwelling (cooler temperature on isopycnals) and upwelling (warmer temperature on isopycnals), respectively, that are generally consistent with our upper water column temperature anomalies. The lower water column anomalies are explained by nonequivalent barotropic flow i.e., the turning of the velocity vector with depth, shown to hold in the Gulf Stream (Lindstrom et al. 1997) and Subantarctic Front (Phillips and Rintoul 2000; Tracey et al. 2006; Phillips and Bindoff 2014). Leading into the trough, the velocity vector turns clockwise (cyclonic) from deep to shallow levels, known as backing, and anticlockwise (anticyclonic) leading into the crest, or veering. This leads to cold advection and downwelling leading into the trough (bcd) and warm advection and upwelling

(uvw) entering the crest. Although these observed temperature changes are in the intermediate depth range, the cold and warm advection there suggests the presence of a deep cyclone about midway between the upper-ocean trough and crest.

In meteorological studies and some recent studies of the Gulf Stream, these observed temperature anomalies are linked to cyclogenesis, where patterns of divergence in the jet stream are connected to convergence (low pressures) at the surface. The opposite is also true; convergence in the jet stream is linked to divergence (high pressures) at the surface. Analogous to the atmosphere, it is quite likely that this view of divergence patterns between the surface and at depth is also valid for meanders of the ACC. The equatorward advection of cold water leading into the trough and poleward advection of warm water leading into the crest causes a net poleward heat transport. This poleward heat flux contributes to the meridional heat transport needed to balance air-sea heat loss around Antarctica and drives ice melt at higher latitudes (Rintoul and Naveira Garabato 2013). The cyclones at depth increase bottom velocities, leading to dissipation of momentum due to the generation of lee waves and bottom friction. Thus, cyclogenesis could be an important contributor to the momentum dissipation needed to explain the near-constant volume transport of the ACC in spite of observed increasing winds (Böning et al. 2008).

**Acknowledgments.** We thank the crew members of the RV *Southern Surveyor*, the RSV *Aurora Australis*, and the *Marine National Facility* for obtaining and making available a unique dataset of a standing meander in the Antarctic Circumpolar Current. This research was supported by the Centre for Southern Hemisphere Oceans Research (CSHOR), a partnership between the Commonwealth Scientific and Industrial Research Organisation (CSIRO) and the Qingdao National Laboratory for Marine Science; the Australian Antarctic Program Partnership; and the Climate Systems and Earth Systems and Climate Change Hub of the Australian Government's National Environmental Science Program. HP and NB acknowledge funding from the Australian Research Council Discovery Projects (DP170102162). We thank the contributors to the GSW-Python/GSW-C packages for making the Gibbs Sea-Water (GSW) Oceanographic Toolbox of TEOS-10 available (<https://github.com/TEOS-10/GSW-Python>), originally written in MATLAB by David Jackett, Trevor McDougall, and Paul Barker (<http://www.teos-10.org>). We also would like to express our appreciation for the comments of two anonymous reviewers, which have greatly improved the manuscript.

**Data availability statement.** Shipboard ADCP and CTD data (SS9802) of the Subantarctic Front meander in the Antarctic Circumpolar Current are found at [https://www.cmar.csiro.au/data/rawler/survey\\_details.cfm?survey=SS199802](https://www.cmar.csiro.au/data/rawler/survey_details.cfm?survey=SS199802) and CTD data from the SR3 transect (AU9706) are found at [https://www.cmar.csiro.au/data/rawler/survey\\_details.cfm?survey=AU199706](https://www.cmar.csiro.au/data/rawler/survey_details.cfm?survey=AU199706) calibrated and quality controlled by CSIRO National Collections and Marine Infrastructure. Satellite altimetry data can be

retrieved from <http://marine.copernicus.eu> and are made available by Copernicus Marine and Environment Monitoring Service. For repeatability and reproducibility of this research, Python scripts are made available in public repositories that can be found at <https://github.com/janjaapmeijer/phd-public> and <https://github.com/janjaapmeijer/oceanpy>.

## REFERENCES

- Armour, K. C., J. Marshall, J. R. Scott, A. Donohoe, and E. R. Newsom, 2016: Southern Ocean warming delayed by circumpolar upwelling and equatorward transport. *Nat. Geosci.*, **9**, 549–554, <https://doi.org/10.1038/ngeo2731>.
- Bindoff, N. L., and T. J. McDougall, 1994: Diagnosing climate change and ocean ventilation using hydrographic data. *J. Phys. Oceanogr.*, **24**, 1137–1152, [https://doi.org/10.1175/1520-0485\(1994\)024<1137:DCCAOV>2.0.CO;2](https://doi.org/10.1175/1520-0485(1994)024<1137:DCCAOV>2.0.CO;2).
- , and —, 2000: Decadal changes along an Indian Ocean section at 32°S and their interpretation. *J. Phys. Oceanogr.*, **30**, 1207–1222, [https://doi.org/10.1175/1520-0485\(2000\)030<1207:DCAAO>2.0.CO;2](https://doi.org/10.1175/1520-0485(2000)030<1207:DCAAO>2.0.CO;2).
- Böning, C. W., A. Dispert, M. Visbeck, S. R. Rintoul, and F. U. Schwarzkopf, 2008: The response of the Antarctic Circumpolar Current to recent climate change. *Nat. Geosci.*, **1**, 864–869, <https://doi.org/10.1038/ngeo362>.
- Bower, A. S., 1989: Potential vorticity balances and horizontal divergence along particle trajectories in Gulf Stream meanders east of Cape Hatteras. *J. Phys. Oceanogr.*, **19**, 1669–1681, [https://doi.org/10.1175/1520-0485\(1989\)019<1669:PVBAHD>2.0.CO;2](https://doi.org/10.1175/1520-0485(1989)019<1669:PVBAHD>2.0.CO;2).
- Chereskin, T. K., K. A. Donohue, D. R. Watts, K. L. Tracey, Y. L. Firing, and A. L. Cutting, 2009: Strong bottom currents and cyclogenesis in Drake Passage. *Geophys. Res. Lett.*, **36**, L23602, <https://doi.org/10.1029/2009GL040940>.
- Cushman-Roisin, B., and J.-M. Beckers, 2011: *Introduction to Geophysical Fluid Dynamics: Physical and Numerical Aspects*. 2nd ed. Academic Press, 875 pp.
- Firing, Y. L., T. K. Chereskin, D. R. Watts, and M. R. Mazloff, 2016: Bottom pressure torque and the vorticity balance from observations in Drake Passage. *J. Geophys. Res. Oceans*, **121**, 4282–4302, <https://doi.org/10.1002/2016JC011682>.
- , E. L. McDonagh, B. A. King, and D. G. Desbruyères, 2017: Deep temperature variability in Drake Passage. *J. Geophys. Res. Oceans*, **122**, 713–725, <https://doi.org/10.1002/2016JC012452>.
- Foppert, A., K. A. Donohue, D. R. Watts, and K. L. Tracey, 2017: Eddy heat flux across the Antarctic Circumpolar Current estimated from sea surface height standard deviation. *J. Geophys. Res. Oceans*, **122**, 6947–6964, <https://doi.org/10.1002/2017JC012837>.
- Frölicher, T. L., J. L. Sarmiento, D. J. Paynter, J. P. Dunne, J. P. Krasting, and M. Winton, 2015: Dominance of the Southern Ocean in anthropogenic carbon and heat uptake in CMIP5 models. *J. Climate*, **28**, 862–886, <https://doi.org/10.1175/JCLI-D-14-00117.1>.
- Fu, L.-L., D. B. Chelton, P.-Y. Le Traon, and R. Morrow, 2010: Eddy dynamics from satellite altimetry. *Oceanography*, **23**, 14–25, <https://doi.org/10.5670/oceanog.2010.02>.
- Gnanadesikan, A., 1999: A simple predictive model for the structure of the oceanic pycnocline. *Science*, **283**, 2077–2079, <https://doi.org/10.1126/science.283.5410.2077>.
- GEBCO Compilation Group, 2019: GEBCO 2019 grid. GEBCO, accessed 29 March 2020, <https://doi.org/10.5285/836f016a-33be-6ddc-e053-6c86abc0788e>.
- Gill, A. E., 1968: A linear model of the Antarctic Circumpolar Current. *J. Fluid Mech.*, **32**, 465–488, <https://doi.org/10.1017/S0022112068000868>.
- Hallberg, R., and A. Gnanadesikan, 2006: The role of eddies in determining the structure and response of the wind-driven Southern Hemisphere overturning: Results from the Modeling Eddies in the Southern Ocean (MESO) project. *J. Phys. Oceanogr.*, **36**, 2232–2252, <https://doi.org/10.1175/JPO2980.1>.
- Herráiz-Borreguero, L., and S. R. Rintoul, 2011: Subantarctic mode water: Distribution and circulation. *Ocean Dyn.*, **61**, 103–126, <https://doi.org/10.1007/s10236-010-0352-9>.
- Hogg, A. M., M. P. Meredith, D. P. Chambers, E. P. Abrahamsen, C. W. Hughes, and A. K. Morrison, 2015: Recent trends in the Southern Ocean eddy field. *J. Geophys. Res. Oceans*, **120**, 257–267, <https://doi.org/10.1002/2014JC010470>.
- Holte, J., and L. Talley, 2009: A new algorithm for finding mixed layer depths with applications to Argo Data and Subantarctic mode water formation. *J. Atmos. Oceanic Technol.*, **26**, 1920–1939, <https://doi.org/10.1175/2009JTECHO543.1>.
- Holton, J. R., 2004: *An Introduction to Dynamic Meteorology*. Academic Press, 535 pp.
- Hughes, C. W., 1995: Rossby waves in the Southern Ocean: A comparison of TOPEX/POSEIDON altimetry with model predictions. *J. Geophys. Res.*, **100**, 15 933–15 950, <https://doi.org/10.1029/95JC01380>.
- , 2005: Nonlinear vorticity balance of the Antarctic Circumpolar Current. *J. Geophys. Res.*, **110**, C11008, <https://doi.org/10.1029/2004JC002753>.
- Jackett, D. R., and T. J. McDougall, 1997: A neutral density variable for the world's oceans. *J. Phys. Oceanogr.*, **27**, 237–263, [https://doi.org/10.1175/1520-0485\(1997\)027<0237:ANDVFT>2.0.CO;2](https://doi.org/10.1175/1520-0485(1997)027<0237:ANDVFT>2.0.CO;2).
- Johnson, G. C., and H. L. Bryden, 1989: On the size of the Antarctic Circumpolar Current. *Deep-Sea Res.*, **36A**, 39–53, [https://doi.org/10.1016/0198-0149\(89\)90017-4](https://doi.org/10.1016/0198-0149(89)90017-4).
- Lindstrom, S. S., X. Qian, and D. R. Watts, 1997: Vertical motion in the Gulf Stream and its relation to meanders. *J. Geophys. Res.*, **102**, 8485–8503, <https://doi.org/10.1029/96JC03498>.
- Meijers, A. J., N. L. Bindoff, and J. L. Roberts, 2007: On the total, mean, and eddy heat and freshwater transports in the Southern Hemisphere of a  $1/8^\circ \times 1/8^\circ$  global ocean model. *J. Phys. Oceanogr.*, **37**, 277–295, <https://doi.org/10.1175/JPO3012.1>.
- , —, and S. R. Rintoul, 2010: Estimating the four-dimensional structure of the Southern Ocean using satellite altimetry. *J. Atmos. Oceanic Technol.*, **28**, 548–568, <https://doi.org/10.1175/2010JTECHO790.1>.
- , —, and —, 2011: Frontal movements and property fluxes: Contributions to heat and freshwater trends in the Southern Ocean. *J. Geophys. Res.*, **116**, C08024, <https://doi.org/10.1029/2010JC006832>.
- Meinen, C. S., and D. R. Watts, 2000: Vertical structure and transport on a transect across the North Atlantic Current near 42°N: Time series and mean. *J. Geophys. Res.*, **105**, 21 869–21 891, <https://doi.org/10.1029/2000JC900097>.
- , D. S. Luther, D. R. Watts, K. L. Tracey, A. D. Chave, and J. Richman, 2002: Combining inverted echo sounder and horizontal electric field recorder measurements to obtain absolute velocity profiles. *J. Atmos. Oceanic Technol.*, **19**, 1653–1664, [https://doi.org/10.1175/1520-0426\(2002\)019<1653:CIESAH>2.0.CO;2](https://doi.org/10.1175/1520-0426(2002)019<1653:CIESAH>2.0.CO;2).

- Meredith, M., and Coauthors, 2019: Polar regions. *IPCC Special Report on the Ocean and Cryosphere in a Changing Climate*, H.-O. Pörtner et al., Eds., Cambridge University Press, 203–320.
- Munk, W. H., and E. Palmén, 1951: Note on the dynamics of the Antarctic Circumpolar Current. *Tellus*, **3**, 53–55, <https://doi.org/10.1111/j.2153-3490.1951.tb00776.x>.
- Naveira Garabato, A. C., R. Ferrari, and K. L. Polzin, 2011: Eddy stirring in the Southern Ocean. *J. Geophys. Res.*, **116**, C09019, <https://doi.org/10.1029/2010JC006818>.
- Newton, C. W., 1959: Synoptic comparisons of jet streams and Gulf Stream systems. *The Atmosphere and the Sea in Motion*, B. Bolin, Ed., Rockefeller University Press, 288–304.
- Nikurashin, M., G. K. Vallis, and A. Adcroft, 2013: Routes to energy dissipation for geostrophic flows in the Southern Ocean. *Nat. Geosci.*, **6**, 48–51, <https://doi.org/10.1038/ngeo1657>.
- Olbers, D., D. Borowski, C. Völker, and J.-O. Wölff, 2004: The dynamical balance, transport and circulation of the Antarctic Circumpolar Current. *Antarct. Sci.*, **16**, 439–470, <https://doi.org/10.1017/S0954102004002251>.
- Orsi, A. H., T. Whitworth, and W. D. Nowlin, 1995: On the meridional extent and fronts of the Antarctic Circumpolar Current. *Deep-Sea Res. I*, **42**, 641–673, [https://doi.org/10.1016/0967-0637\(95\)00021-W](https://doi.org/10.1016/0967-0637(95)00021-W).
- , W. M. Smethie, and J. L. Bullister, 2002: On the total input of Antarctic waters to the deep ocean: A preliminary estimate from chlorofluorocarbon measurements. *J. Geophys. Res.*, **107**, 3122, <https://doi.org/10.1029/2001JC000976>.
- Palmén, E. H., and C. W. Newton, Eds., 1969: *Atmospheric Circulation Systems: Their Structure and Physical Interpretation*. International Geophysics, Vol. 13, Academic Press, 603 pp.
- Phillips, H. E., and S. R. Rintoul, 2000: Eddy variability and energetics from direct current measurements in the Antarctic Circumpolar Current South of Australia. *J. Phys. Oceanogr.*, **30**, 3050–3076, [https://doi.org/10.1175/1520-0485\(2000\)030<3050:EVAEFD>2.0.CO;2](https://doi.org/10.1175/1520-0485(2000)030<3050:EVAEFD>2.0.CO;2).
- , and N. L. Bindoff, 2014: On the nonequivalent barotropic structure of the Antarctic Circumpolar Current: An observational perspective. *J. Geophys. Res. Oceans*, **119**, 5221–5243, <https://doi.org/10.1002/2013JC009516>.
- Rhein, M., and Coauthors, 2013: Observations: Ocean. *Climate Change 2013: The Physical Science Basis*, T. Stocker et al., Eds., Cambridge University Press, 255–316.
- Rintoul, S. R., and J. L. Bullister, 1999: A late winter hydrographic section from Tasmania to Antarctica. *Deep-Sea Res. I*, **46**, 1417–1454, [https://doi.org/10.1016/S0967-0637\(99\)00013-8](https://doi.org/10.1016/S0967-0637(99)00013-8).
- , and A. C. Naveira Garabato, 2013: Dynamics of the Southern Ocean circulation. *Ocean Circulation and Climate: A 21st Century Perspective*, G. Siedler, J. Gould, and J. A. Church, Eds., International Geophysics, Vol. 103, Academic Press, 471–492.
- Savidge, D. K., and J. M. Bane, 1999a: Cyclogenesis in the deep ocean beneath the Gulf Stream: 1. Description. *J. Geophys. Res.*, **104**, 18 111–18 126, <https://doi.org/10.1029/1999JC900132>.
- , and —, 1999b: Cyclogenesis in the deep ocean beneath the Gulf Stream: 2. Dynamics. *J. Geophys. Res.*, **104**, 18 127–18 140, <https://doi.org/10.1029/1999JC900131>.
- Schubert, R., A. Biastoch, M. F. Cronin, and R. J. Greatbatch, 2018: Instability-driven benthic storms below the separated Gulf Stream and the North Atlantic Current in a high-resolution ocean model. *J. Phys. Oceanogr.*, **48**, 2283–2303, <https://doi.org/10.1175/JPO-D-17-0261.1>.
- Sloyan, B. M., and S. R. Rintoul, 2001: Circulation, renewal, and modification of Antarctic Mode and intermediate water. *J. Phys. Oceanogr.*, **31**, 1005–1030, [https://doi.org/10.1175/1520-0485\(2001\)031<1005:CRAMOA>2.0.CO;2](https://doi.org/10.1175/1520-0485(2001)031<1005:CRAMOA>2.0.CO;2).
- Straub, D. N., 1993: On the transport and angular momentum balance of channel models of the Antarctic Circumpolar Current. *J. Phys. Oceanogr.*, **23**, 776–782, [https://doi.org/10.1175/1520-0485\(1993\)023<0776:OTTAAM>2.0.CO;2](https://doi.org/10.1175/1520-0485(1993)023<0776:OTTAAM>2.0.CO;2).
- Thompson, A. F., and J.-B. Sallée, 2012: Jets and topography: Jet transitions and the impact on transport in the Antarctic Circumpolar Current. *J. Phys. Oceanogr.*, **42**, 956–972, <https://doi.org/10.1175/JPO-D-11-0135.1>.
- , and A. C. Naveira Garabato, 2014: Equilibration of the Antarctic Circumpolar Current by standing meanders. *J. Phys. Oceanogr.*, **44**, 1811–1828, <https://doi.org/10.1175/JPO-D-13-0163.1>.
- Thompson, D. W. J., S. Solomon, P. J. Kushner, M. H. England, K. M. Grise, and D. J. Karoly, 2011: Signatures of the Antarctic ozone hole in Southern Hemisphere surface climate change. *Nat. Geosci.*, **4**, 741–749, <https://doi.org/10.1038/ngeo1296>.
- Tracey, K. L., D. R. Watts, C. S. Meinen, and D. S. Luther, 2006: Synoptic maps of temperature and velocity within the Subantarctic Front south of Australia. *J. Geophys. Res.*, **111**, C10016, <https://doi.org/10.1029/2005JC002905>.
- Watts, D. R., C. Sun, and S. Rintoul, 2001: A two-dimensional gravest empirical mode determined from hydrographic observations in the subantarctic front. *J. Phys. Oceanogr.*, **31**, 2186–2209, [https://doi.org/10.1175/1520-0485\(2001\)031<2186:ATDGEM>2.0.CO;2](https://doi.org/10.1175/1520-0485(2001)031<2186:ATDGEM>2.0.CO;2).
- , K. L. Tracey, K. A. Donohue, and T. K. Chereskin, 2016: Estimates of eddy heat flux crossing the Antarctic Circumpolar Current from observations in Drake Passage. *J. Phys. Oceanogr.*, **46**, 2103–2122, <https://doi.org/10.1175/JPO-D-16-0029.1>.